Journal of Materials Research and Technology 32 (2024) 817–826

Contents lists available at ScienceDirect

Journal of Materials Research and Technology

journal homepage: www.elsevier.com/locate/jmrt

A new cohesive-based modelling of moisture-dependent mode II delamination of carbon/epoxy composites

M.N. Mohd Fua'ad [a], K.J. Wong [b,*], H.A. Israr [a], T. Dickhut [c], S.S. R. Koloor [c,**]

[a] Faculty of Mechanical Engineering, Universiti Teknologi Malaysia, 81310, UTM Skudai, Johor, Malaysia
[b] Department of Mechanical, Materials and Manufacturing Engineering, Faculty of Science and Engineering, University of Nottingham Malaysia, Jalan Broga, 43500, Semenyih, Selangor, Malaysia
[c] Chair of Composite Materials and Technical Mechanics, Institute of Aeronautical Engineering, Faculty of Mechanical Engineering, Universität der Bundeswehr München, Werner-Heisenberg-Weg 39, 85579, Neubiberg, Munich, Germany

ARTICLE INFO

Handling editor: SN Monteiro

Keywords:
Carbon/Epoxy composite
Moisture absorption
Mode II delamination
Cohesive zone model
Residual property model

ABSTRACT

The cohesive zone model (CZM) is widely employed for simulating delamination and debonding behaviour in engineering structures. However, the choice of CZM shape impacts the accuracy of simulation results. Therefore, the selection of a suitable Traction-Separation Law (TSL) with appropriate cohesive parameters is crucial. This study focuses on simulating the mode II delamination of unidirectional carbon/epoxy composites under varying moisture content levels (0%, 2.2%, 3.8%, and 5.3%) using the End Notched Flexure (ENF) test. Trapezoidal TSL (TTSL) with varying pseudo-plasticity parameter (Γ) was implemented and compared. A guideline was proposed in this study to aid in the selection of cohesive parameters, and a relationship between these parameters and moisture content was established. The results indicate that $\Gamma = 0.99$ yields a more accurate force-displacement response compared to $\Gamma = 0$. The estimated cohesive zone length falls within the range of 2.0–2.4 mm. During crack growth, the analysis reveals that, at the peak force, a region approximately 0.5–0.6 mm ahead of the crack tip undergoes total failure. Simultaneously, damage initiation occurs in the region 2.3–2.4 mm beyond the complete failure zone.

1. Introduction

Advanced composites and their damage mechanics process have become one of the core subjects of studies in fracture mechanics, demanded for the design of aerospace composite parts [1]. Interlaminar damage and fracture are classified as one of the primary failure phenomena threaten structural integrity for many different applications [2,3]. The Cohesive Zone Model (CZM) has become a prominent tool for simulating delamination behaviour in composite laminates and adhesive joints in recent decades. Finite element simulations utilising CZM offer valuable insights into stress states, damage initiation, and growth, providing an alternative to extensive and complex experimental setups. The choice of CZM shape, which is described by the traction-separation law (TSL), significantly influences simulation accuracy [4,5]. The bilinear TSL (BTSL) is widely adopted for its simplicity and accuracy, especially in modelling brittle and moderately ductile materials [6]. Publications that utilised BTSL included [7–20]. However, its applicability is not universal. For instance, BTSL was found to be suitable for the brittle adhesive, while exponential TSL (ETSL) was suitable for ductile adhesive bonded butt joints under tensile and shear loadings [4]. ETSL has also been implemented for Ti/silicon carbide interfaces [21], while some other types of TSL include trapezoidal [4,22–29], trilinear [30–33], bilinear-exponential [34], tetra-linear [35], polynomial [36], linear-parabolic [37], and multilinear [38]. Among these, trapezoidal TSL (TTSL) has proven successful in simulating delamination behaviour, particularly in interfaces exhibiting non-linear fracture behaviour [26] and elastic-plastic behaviour, where ductility was to be considered [22–25]. May et al. [39] proposed that the plateau region of the TTSL needed to be enlarged with the plasticity to accommodate the increased ductility.

Several studies have applied TTSL to investigate mode II delamination. For example, Tauheed and Datla [40] conducted an investigation on the mode II delamination of unidirectional carbon fibre composites bonded to Araldite AV138 epoxy adhesive using End Notched Flexure

* Corresponding author.
** Corresponding author.
E-mail addresses: kingjye.wong@nottingham.edu.my (K.J. Wong), seyed.rahimian@unibw.de (S.S. R. Koloor).

https://doi.org/10.1016/j.jmrt.2024.07.197
Received 12 May 2024; Received in revised form 22 July 2024; Accepted 24 July 2024
Available online 26 July 2024

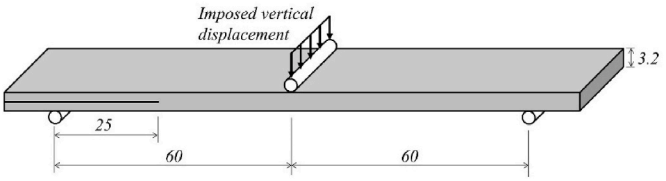

Fig. 1. Schematic diagram of the mode II end-notched flexure test setup.

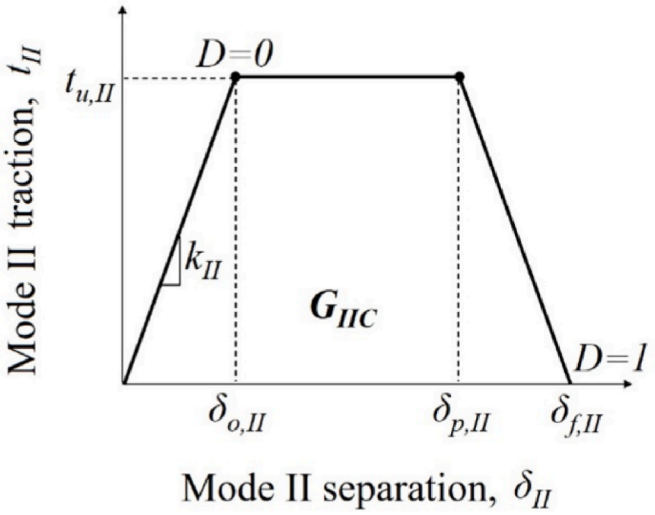

Fig. 2. Schematic diagram of the pure mode II trapezoidal traction-separation law.

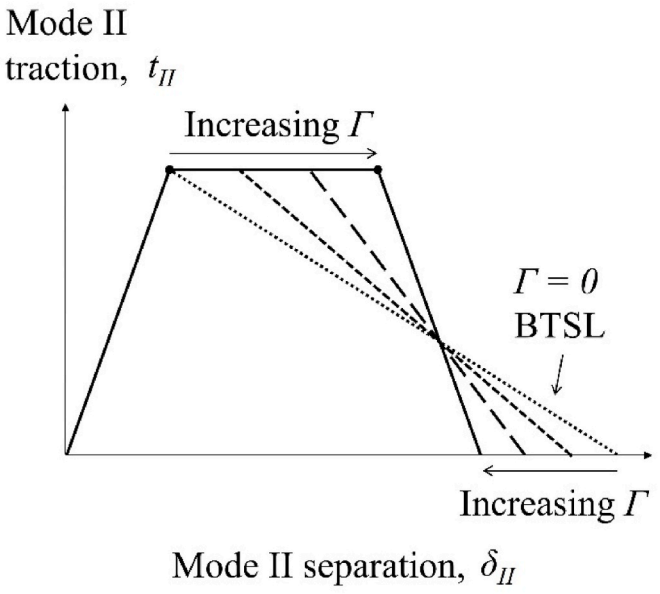

Fig. 3. Variation of trapezoidal traction-separation law with the pseudo-plasticity parameter (Γ).

(ENF) specimens. These specimens underwent ageing at 40 °C and 82% relative humidity (RH). The mode II separation was directly determined through digital image correlation (DIC) of crack tip images, utilising open-faced specimens. By establishing the relationship between the mode II energy release rate, $G_{II,}$ and separation, δ_{II}, the traction was derived by differentiating G_{II} with respect to δ_{II}. Subsequently, cohesive parameters for TTSL were developed for all ageing conditions. The

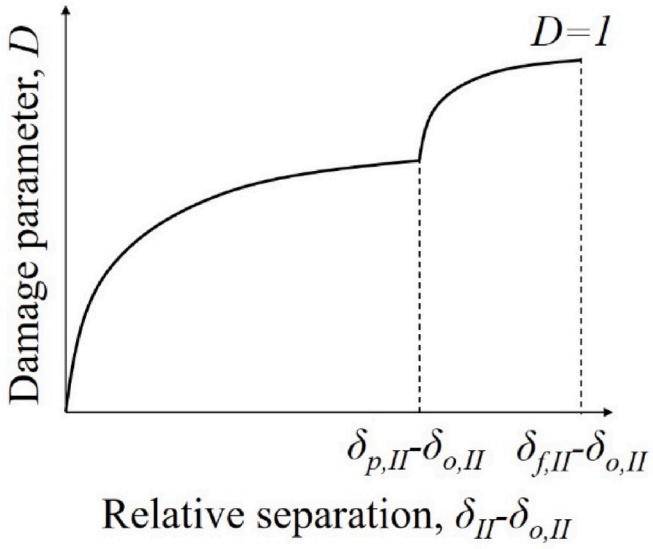

Fig. 4. Damage parameter evolution of trapezoidal traction-separation law.

Table 1
Interface properties used in trapezoidal traction-separation law.

M (%)	G_{IIC} *(N/mm)* [47]	k_{II} *(MPa/mm)*	$t_{u,II}$ *(MPa)*	$\delta_{o,II}$ (× 10^{-4} *mm)*	$\delta_{p,II}$ (× 10^{-2} *mm)* (Γ = 0.99)	$\delta_{f,II}$ (× 10^{-2} *mm)*
Dry	2.06	4.5 × 10^5	100	2.22	2.06	2.08
2.2	1.39		82	1.83	1.69	1.71
3.8	1.02		71	1.57	1.45	1.47
5.3	0.92		67	1.48	1.37	1.39

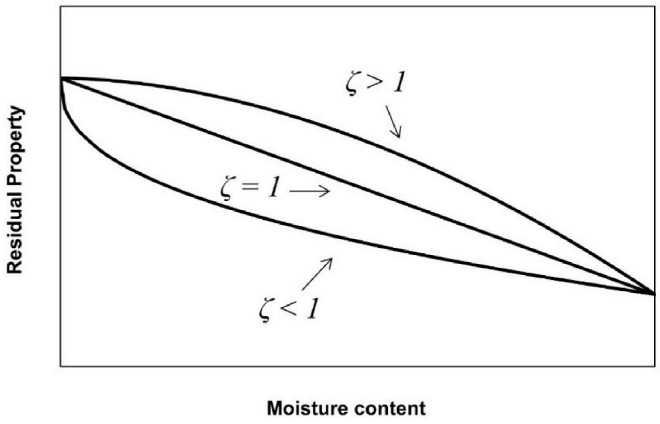

Fig. 5. Degradation trends of the residual property with respect to the moisture content.

validity of these cohesive parameters was confirmed through good agreement when comparing results with closed specimens, providing robust support for the model's accuracy and reliability.

Anyfantis and Tsouvalis [41] conducted a study on mode II delamination in unidirectional glass/epoxy composites using ENF specimens. Crack growth was monitored with a high-resolution video camera. Following a procedure similar to Tauheed and Datla [40], the traction was computed by differentiating G_{II} with respect to δ_{II}. The outcomes from the TTSL, which encompassed both initiation and bridging fracture energy, demonstrated a favourable comparison between experimental and numerical force-displacement curves. This suggests that TTSL

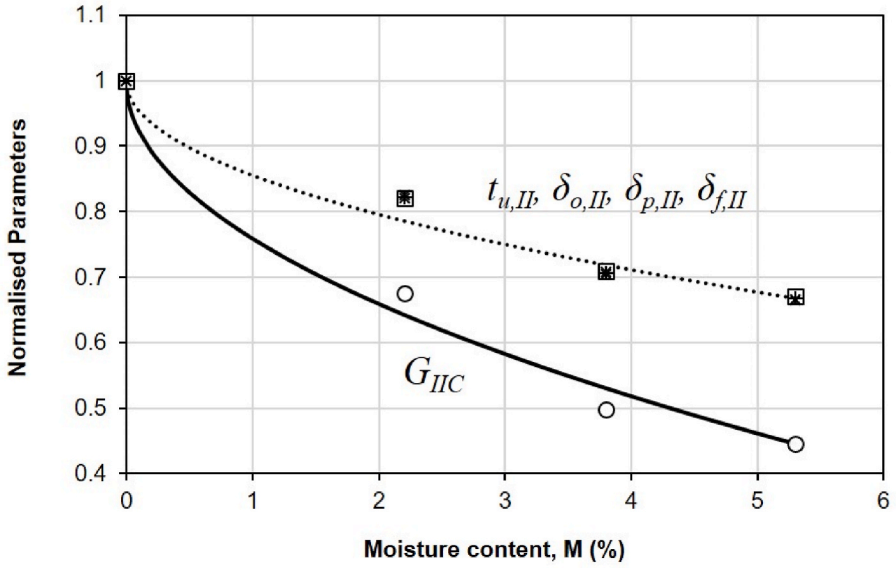

Fig. 6. Variation of mode II fracture toughness and cohesive parameters with respect to moisture content.

Table 2
Normalised interface properties used in trapezoidal traction-separation law.

M (%)	G_{IIC}	$t_{u,II}$	$\delta_{o,II}$	$\delta_{p,II}$	$\delta_{f,II}$
Dry	1	1	1	1	1
2.2	0.68	0.82	0.82	0.82	0.82
3.8	0.50	0.71	0.71	0.70	0.71
5.3	0.45	0.67	0.67	0.67	0.67

effectively captured the essential aspects of the mode II delamination behaviour in the glass/epoxy composites under investigation.

Ghabezi and Farahani [42] undertook a characterisation of mode II delamination in nano-alumina powder-reinforced Araldite 2015 adhesive bonded nano–glass/epoxy composite joints, utilising ENF specimens. TTSL was implemented to account for the R-curve of the specimens. Their findings indicated that the introduction of nanoparticles led to an increase in both initiation and plateau values of the mode II energy release rate. Furthermore, it was observed that the mode II interface strength demonstrated an initial increase with the addition of nanoparticles in the adhesive, specifically in the range of 0–0.5 wt%. However, beyond this concentration, a subsequent decrease in the mode II interface strength was noted. This suggests a nuanced influence of nanoparticle content on the delamination characteristics of the composite joints.

Owing to the non-linear fracture behaviour observed in experiments, TTSL was employed to assess the delamination behaviour of a honeycomb/carbon-epoxy sandwich structure [43] using the asymmetric ENF (AENF) test [26]. The investigation revealed that mode II predominantly influenced the delamination occurring between the skin and the core. Employing a numerical inverse procedure, the authors successfully demonstrated a robust comparison between the experimental and numerical force-displacement curves as well as R-curves.

Al-Azzawi et al. [22] conducted a study on the flexural behaviour of asymmetric Glare 4B fibre-metal laminates (FMLs) featuring doubler joint configurations, using a four-point bending test. The composite

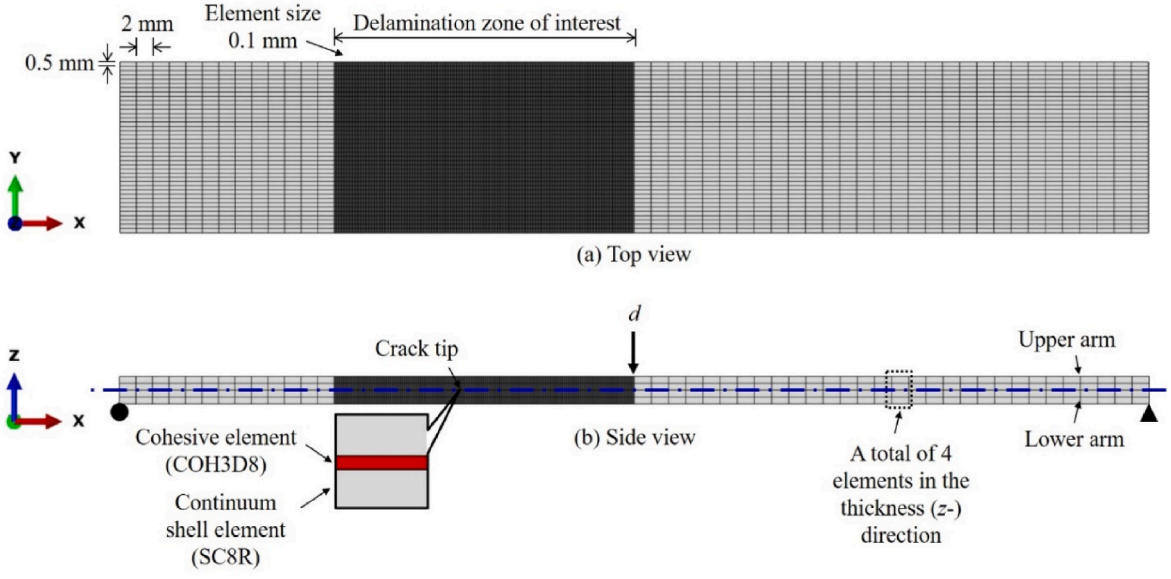

Fig. 7. Finite element model of the composite for mode II delamination under three-point end-notched flexure loading: (a) side and (b) top view.

Table 3
Lamina properties for the carbon fibre reinforced epoxy composite [49].

M (%)	E_{11} (GPa)	E_{22} (GPa)	G_{12} (GPa)	G_{13} (GPa)[a]	G_{23} (GPa)[a]	ν_{12}
0	103.0	6.7	2.7	2.7	2.5	0.34
2.2	97.0	4.6	2.7	2.7	2.5	0.34
3.8	96.0	4.3	2.6	2.6	2.3	0.36
5.3	95.0	4.5	2.5	2.5	2.2	0.37

[a] Assumed values, derived by further refinement.

utilised was unidirectional S2 glass/epoxy, while the metal component was aluminium. To model the interlaminar layer between the composite and aluminium under through-thickness compressive stress, a modified CZM was developed. This new CZM was presented as TTSL, considering the elastic-plastic damage behaviour due to toughened epoxy. In addition to the ductile damage in the FM94 epoxy, the numerical modelling also accounted for damage in the composite and plasticity in the Al. Results indicated that the modified CZM predicted a more accurate force-deflection behaviour compared to the unmodified version. Moreover, TTSL was successfully applied to simulate delamination propagation in the same FMLs, featuring both splice and doubler configurations, under static and fatigue loadings [23].

Furthermore, TTSL has been applied to address mode I delamination which has normally been done using Double Cantilever Beam (DCB) test [44]. Watson et al. [45], for example, extracted the TTSL from the rigid Double Cantilever Beam (RDCB) test using high stiffness steel as the adherend and 3 M impact-resistant 7333 structural epoxy as the adhesive. The experimental and numerical force-displacement responses were effectively compared. Subsequently, the authors employed the same TTSL methodology in the tapered DCB (TDCB) test, achieving a successful comparison between the experimental and numerical force-displacement profiles.

Moslemi-Abyane and Ghasemi [46] conducted a study on the impact of thermal cycle loading on mode I delamination in unidirectional E-glass fibre-reinforced epoxy composites, utilising DCB specimens. The specimens underwent thermal cycling between 15 and 65 °C for 50, 100,

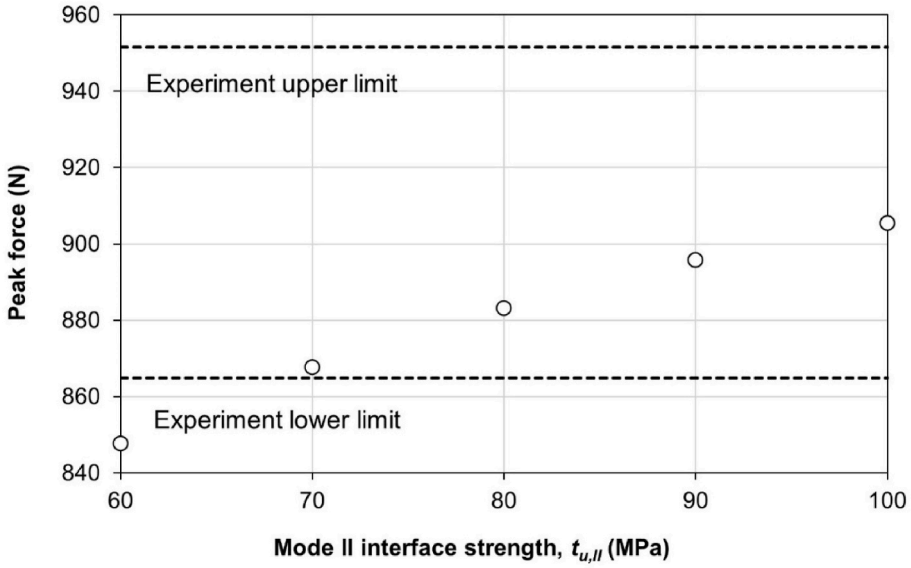

Fig. 8. Influence of the mode II interface strength on the numerical peak force for dry specimens using $\Gamma = 0$.

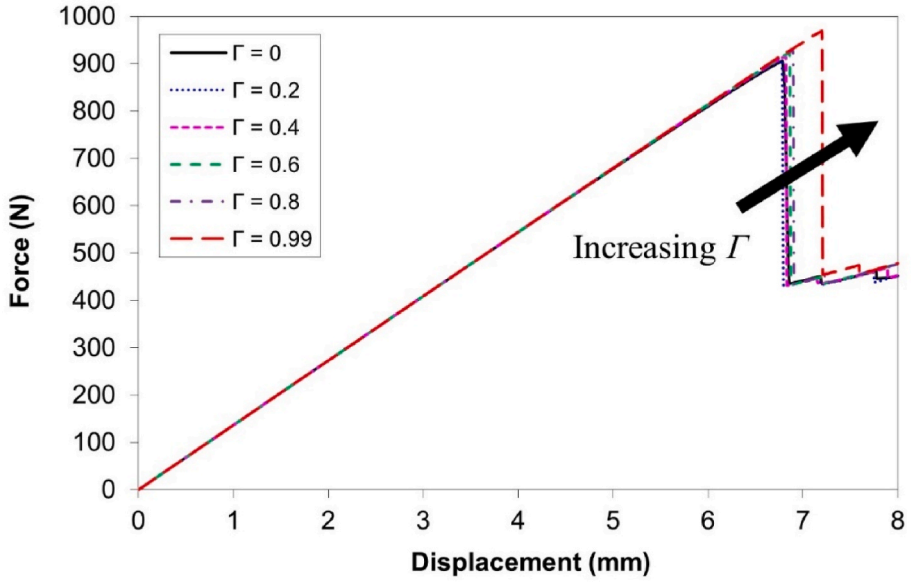

Fig. 9. Influence of the pseudo-plasticity parameter on the numerical force-displacement curve at dry condition.

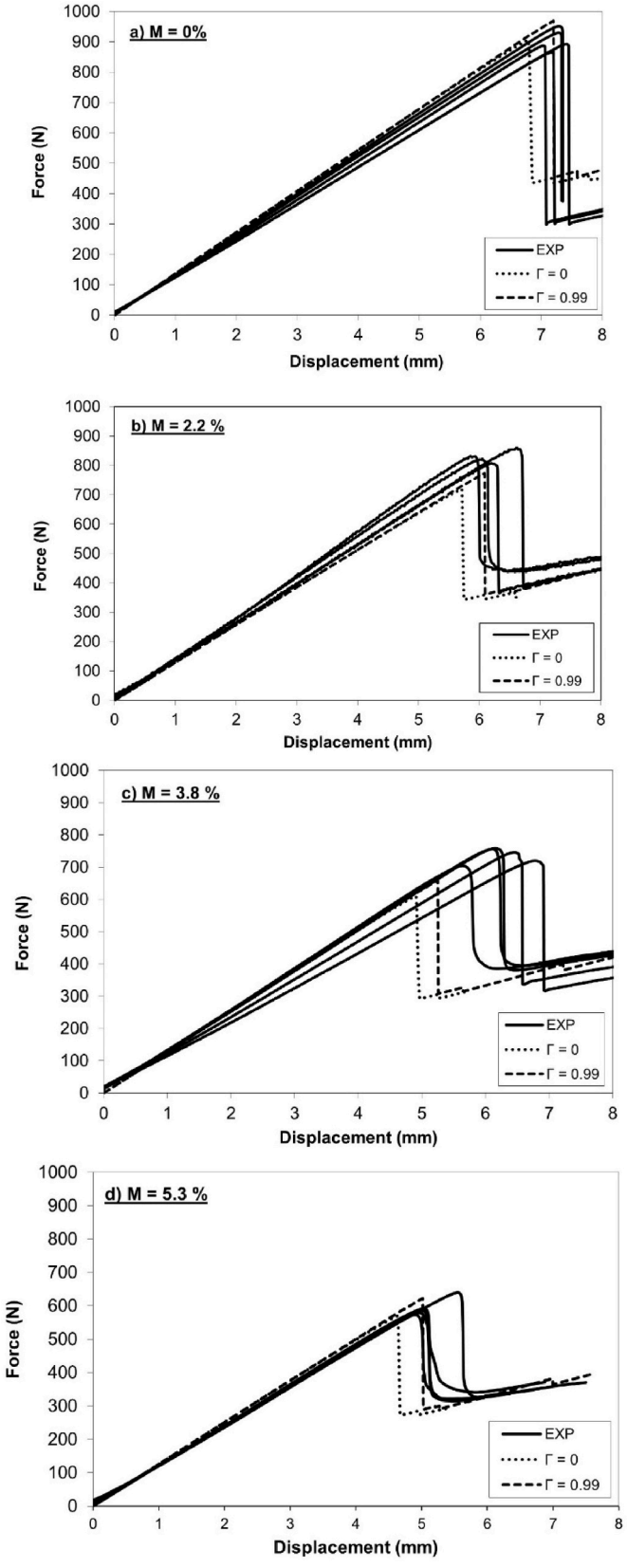

Fig. 10. Results of force-displacement curves obtained through experiment and numerical simulation of the samples under mode II delamination at moisture content levels of (a) $M = 0$ %, (a) $M = 2.2$ %, (a) $M = 3.8$ %, and (d) $M = 5.3$ %.

and 150 cycles. Notably, thermal cycling resulted in premature damage to the composite structures. The crack tip opening displacement (CTOD) was measured using DIC, while the traction was quantified by differentiating the mode I strain energy release rate, G_I with respect to the CTOD, δ_I. It is essential to highlight that the same procedure was employed for mode II delamination, as detailed in the preceding paragraphs [40,41]. Over here, TTSL was incorporated to account for the fibre bridging phenomenon. Analysis of the cohesive parameters revealed that an increase in the number of thermal cycles reduced the separation at failure but concurrently increased local traction. This observation suggested that thermal cycling induced brittleness in the composite material, leading to a decrease in absorbed energy.

Recently, Noruzi and Khoramishad [24] introduced an equivalent TTSL (ETTSL) for broad applicability with both ductile and brittle adhesives bonded to various substrate materials. The model's versatility was demonstrated by its initial application in characterising the mode I delamination behaviour of ductile polyurethane (PU) adhesive bonded to woven E-glass/epoxy composite joints, employing the DCB test. Subsequent validations were conducted using data from existing literature, revealing a consistently good comparison across all cases. This promising outcome highlights the ETTSL model's potential to streamline and economise complex analyses, particularly when compared to the conventional CZM.

The literature discussed above highlights the versatility of TTSL, demonstrating its suitability for implementation across various materials under diverse loading and environmental conditions. Previous research has shown that fracture toughness was influenced by the moisture content [47]. Specifically, in wet specimens, mode I fibre bridging behaviour has been effectively described using a bilinear-exponential TSL [34]. While mode II did not exhibit fibre bridging, noticeable changes in the fracture surface were observed, suggesting potential degradation of the interface due to moisture attack [47]. Therefore, it is hypothesised that TTSL could serve as an appropriate TSL to characterise mode II delamination under different moisture content levels.

In this study, finite element (FE) modelling was employed to investigate mode II delamination in unidirectional carbon/epoxy composite laminates with varying moisture content. The CZM was adopted, incorporating TTSL at varying pseudo-plasticity parameter (Γ). A systematic guideline was proposed for estimating cohesive parameters. Numerical force-displacement curves were generated for different moisture content levels ($M = 0$, 2.2, 3.8, and 5.3%), and these were compared with experimental data obtained from Ref. [47]. Subsequently, the cohesive zone length was estimated, and the crack growth behaviour was analysed.

2. Materials and methods

This section outlines the experimental details of the mode II ENF test [48], as previously documented in Ref. [47]. Initially, two 16-ply unidirectional carbon/epoxy composite plates (supplied by Structil) measuring 400 × 400 × 3.2 mm^3 were fabricated by using hand lay-out technique. Pre-cracks were induced by inserting a 15 μm-thick Teflon film at the mid-plane of the plates. Subsequently, each composite plate was halved, resulting in four smaller plates measuring 400 × 200 × 3.2 mm^3. Three of the plates were immersed in distilled water at 70 °C, while the fourth was tested under dry condition. After immersion periods of 1, 3, and 9 months, corresponding to moisture gains of $M =$ 2.2%, 3.8% and 5.3%, the plates were removed from the water bath. Specimens with a width of 20 mm were then cut from each plate for mode II ENF test. Fig. 1 depicts the schematic of the ENF test setup, where the thickness of each specimen was 3.2 mm, the initial crack length was 25 mm, and the half span length was fixed at 60 mm. Tests were conducted under displacement control using a universal testing machine equipped with a 5 kN capacity load cell at a crosshead speed of 1 mm/min. At least four specimens were tested for each moisture

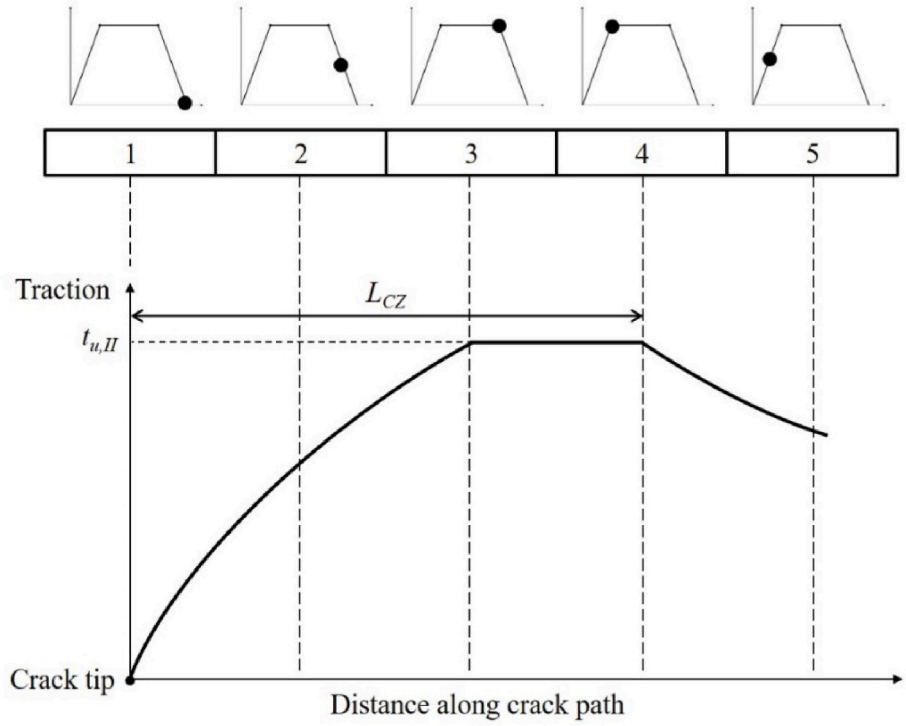

Fig. 11. Traction profile and cohesive zone length of trapezoidal traction-separation law.

content.

3. Cohesive zone model

3.1. Trapezoidal traction-separation law

Fig. 2 delineates the pure mode II TTSL. During the early stage, the shear traction, t_{II} exhibits a linear increase with the relative separation, δ_{II}. The slope of this linear region represents the mode II interface stiffness, k_{II}. Upon reaching the mode II interface strength, $t_{u,II}$, which corresponds to the relative separation $\delta_{o,II}$, damage is initiated ($D = 0$). Subsequent increment in δ_{II} results in a constant value of t_{II}. This region is indicative of the plasticity effect on the interface. $\delta_{p,II}$ indicates the second inflexion point of the trapezoidal law. Beyond this plateau, the traction diminishes linearly. Once δ_{II} equals $\delta_{f,II}$, the element undergoes complete damage, denoted by $t_{II} = 0$ and $D = 1$.

According to May et al. [39], $\delta_{p,II}$ could be expressed as:

$$\delta_{p,II} = \delta_{o,II} + \Gamma \frac{G_{IIC}}{t_{u,II}} \tag{1}$$

In Equation (1), Γ represents the pseudo-plasticity parameter. Fig. 3 shows that increasing Γ signifies higher plasticity level and a reduction in $\delta_{f,II}$. In other words, increasing plasticity leads to a more rapid decline in the traction within the softening zone. In addition, it is noteworthy that when $\Gamma = 0$, the model simplifies to BTSL. To assess the influence of Γ on simulation results, several cases were examined, which included $\Gamma = 0$, 0.2, 0.4, 0.6, 0.8, and 0.99. Specifically, $\Gamma = 0.99$ corresponds to the scenario where the slope of softening region has the same magnitude as k_{II}.

The traction is defined by:

$$t_{II} = \begin{cases} k_{II}\delta_{II} & for \quad 0 \le \delta_{II} \le \delta_{o,II} \\ k_{II}\delta_{o,II} & for \quad \delta_{o,II} < \delta_{II} \le \delta_{p,II} \\ (1-D)k_{II}\delta_{II} & for \quad \delta_{p,II} < \delta_{II} \le \delta_{f,II} \end{cases} \tag{2}$$

The damage parameter, D can be defined as:

$$D = \begin{cases} 1 - \dfrac{\delta_{o,II}}{\delta_{II}} & for \quad \delta_{o,II} \le \delta_{II} \le \delta_{p,II} \\ \dfrac{\delta_{o,II}\left(\delta_{f,II} - \delta_{II}\right)}{\delta_{II}\left(\delta_{f,II} - \delta_{p,II}\right)} & for \quad \delta_{p,II} \le \delta_{II} \le \delta_{f,II} \end{cases} \tag{3}$$

The evolution of D with respect to the relative separation, $\delta_{II} - \delta_{o,II}$ for TTSL is schematically depicted in Fig. 4. It is evident that two distinct regions characterise the evolution of the damage parameter, as indicated by two different equations expressed in Equation (3).

3.2. Determination of the cohesive parameters

Similar to mode I for the same material [34], the mode II penalty stiffness, k_{II} is estimated using Equation (4),

$$k_{II} = \frac{E_m}{h_{ce}} \tag{4}$$

where E_m is the Young's modulus of the epoxy resin (4.5 GPa) and h_{ce} denotes the thickness of the cohesive element (10 μm). The estimated k_{II} is consistently determined to be 4.5×10^5 MPa/mm across all moisture content levels [34]. This determination is based on experimental mode II force-displacement curves, which illustrated a comparable initial linear slope among specimens at different moisture content levels [47]. Furthermore, it has been documented that at various moisture levels, M = 0, 2.2, 3.8, and 5.3%, the experimental longitudinal stiffness, E_{11} values were 105, 97, 96 and 95 GPa, respectively [49], falling within a 10% variation range.

The interface strength is estimated using the relationship shown in Equation (5), which has proven effective for assessing the interface strength across various moisture content levels [10]. The dry mode II interface strength, $t_{u,II,dry}$ is estimated at 100 MPa following a thorough parametric study, detailed in the subsequent section. The resulting interface strength and separations for each moisture condition are computed and summarised in Table 1.

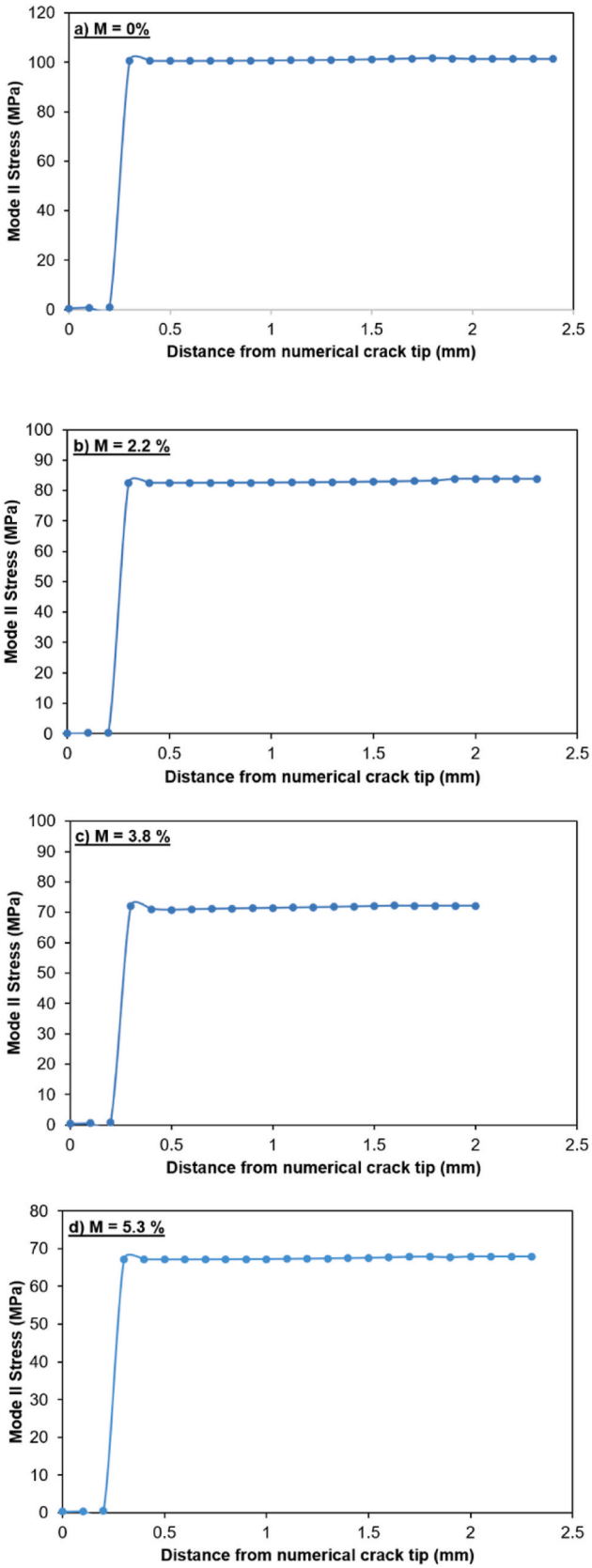

Fig. 12. The cohesive zone length under mode II delamination with moisture content levels of (a) $M = 0$ %, (a) $M = 2.2$ %, (a) $M = 3.8$ %, and (d) $M = 5.3$ %.

Table 4
Cohesive zone length of different moisture content levels for mode II delamination.

Moisture content, M (%)	0	2.2	3.8	5.3
Cohesive zone length, L_{CZ} (mm)	2.4	2.3	2.0	2.3
Number of elements in cohesive zone, N_e	24	23	20	23

$$t_{u,II}(M) = t_{u,II,dry}\sqrt{\frac{G_{IIC}(M)}{G_{IIC,dry}}} \tag{5}$$

The variation of G_{IIC} corelated to M is fitted using the residual property model [10]:

$$\frac{G_{IIC}(M)}{G_{IIC,dry}} = \left[1 - \left(\frac{G_{IIC,min}}{G_{IIC,dry}}\right)\left(\frac{M}{M_{max}}\right)^{\zeta}\right] \tag{6}$$

In Equation (6), $G_{IIC}(M)$ represents the mode II fracture toughness at any moisture content, $G_{IIC,dry}$ is the mode II fracture toughness under dry condition, $G_{IIC,min}$ is lowest mode II fracture toughness (within the range of study), M signifies any moisture content, M_m denotes the maximum moisture content, and ζ is the degradation parameter. This model assumes that G_{IIC} is solely dependent on M. Fig. 5 describes the three possible degradation trends, where $\zeta > 1$ indicates an initial stable value followed by a rapid degradation, $\zeta < 1$ suggests a significant decrement at the early stage but gradually level off at higher moisture content, and $\zeta = 1$ represents a linear degradation. Using $\zeta = 0.5$, the solid line in Fig. 6 fits exceptionally well with a discrepancy of less than 7%. As shown in Fig. 5, a ζ value below unity indicates that G_{IIC} is sensitive to moisture attack. It is important to note that neither Equation (5) nor Equation (6) is derived from physical laws. They are introduced to describe the relationship between the interface strength and fracture energy under dry and wet conditions. This approach minimises the need for computationally intensive calibration of cohesive parameters.

Derived from Equation (5), it is evident to pustulate that the cohesive parameters of $t_{u,II}$, $\delta_{o,II}$, $\delta_{p,II}$, and $\delta_{f,II}$ can be effectively fitted by taking the square root of the term $\left(\frac{G_{IIc,min}}{G_{IIc,dry}}\right)$. Representing all these cohesive parameters collectively as P, the relationship is expressed as follows:

$$\frac{P(M)}{P_{dry}} = \left[1 - \sqrt{\left(\frac{G_{IIc,min}}{G_{IIc,dry}}\right)}\left(\frac{M}{M_{max}}\right)^{\zeta}\right] \tag{7}$$

Maintaining the constant value of ζ, the normalised interface properties are listed in Table 2 while the dotted line, representing the fitted curve, is plotted in Fig. 6. A high level of agreement is observed, with a maximum difference of less than 8%.

4. Finite element modelling

Fig. 7 shows the finite element model of the ENF specimen. Fig. 7(a) illustrates that the composite laminate was modelled using continuum shell elements (SC8R). The mid-plane interface was modelled using cohesive elements (COH3D8) with a cohesive layer thickness set at 10 μm. In the thickness direction (z-axis) of the composite, a total of four elements were discretised. For the imposition of boundary conditions, a roller condition was applied at the bottom-left end, while the right end was fixed with a pinned condition. To emulate the experimental setup, a vertical displacement was introduced at the specimen's midpoint, serving as the designated loading condition.

Along the length of the specimen, Fig. 7(b) shows that the delamination zone of interest was discretised with fine mesh at 0.1 mm. The elements outside the delamination zone of interest were coarser at 2 mm. In the width direction, the specimen was discretised at 0.5-mm mesh. It has been demonstrated that the above-mentioned modelling methodology was sufficient to provide accurate simulation results [8,

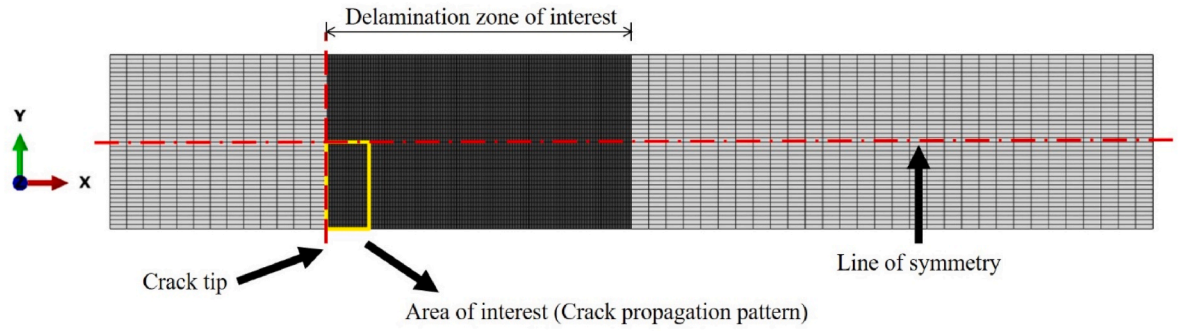

Fig. 13. Area of interest to analyse the crack propagation pattern.

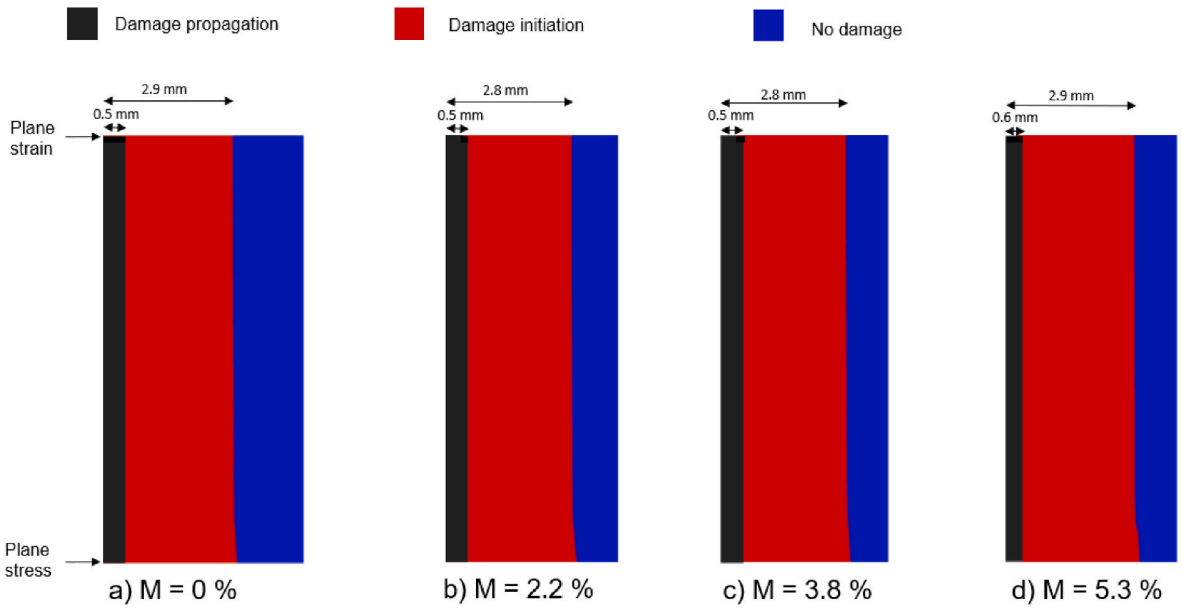

Fig. 14. The crack propagates on the black region, and the damage initiation criterion is met on the red region at the peak load time frame for moisture content of (a) $M = 0$ %, (b) $M = 2.2$ %, (c) $M = 3.8$ %, (d) $M = 5.3$ %.

10]. Table 3 lists the lamina properties of the carbon/epoxy composite at different M levels [49].

5. Results and discussion

5.1. Effects of mode II interface strength

Fig. 8 compares the numerical peak force under different mode II interface strength values, $t_{u,II}$ at the dry condition using BTSL ($\Gamma = 0$). The graph includes upper and lower limits corresponding to experimental peak forces. Notably, as $t_{u,II}$ increases, the numerical peak force also rises. However, even at the upper limit of $t_{u,II} = 100$ MPa, as summarised by Zhao et al. [14], the numerical peak force falls approximately in the middle of the experimental peak force range. This limits accurate estimations at other moisture content levels. Therefore, it is necessary to incorporate plasticity into the CZM to improve the accuracy of the simulation results.

5.2. Effects of pseudo-plasticity parameter

Fig. 9 compares the influence of the pseudo-plasticity parameter, Γ on the numerical force-displacement curves under dry conditions, with $t_{u,II}$ fixed at 100 MPa in all cases. Increasing Γ leads to a slight increase in the numerical peak force, however, this effect is minimal. Compared to $\Gamma = 0$, the maximum difference observed ($\Gamma = 0.99$) is approximately 4%. Furthermore, Γ has negligible influence on the slope of the force-displacement graph. In all cases, there were no instances of instability or convergence issues. Based on these observations, it is postulated that the simulations in this study are insensitive to Γ. As suggested by de Moura et al. [25], in such scenarios, $\delta_{p,II}$ can be effectively modelled by matching the slope of the softening region with that of the initial linear region. Therefore, $\Gamma = 0.99$ is used consistently for all cases across varying moisture content levels.

5.3. Force-displacement curves

In Fig. 10(a)–(d) the force-displacement curves present a comprehensive comparison between experimental and numerical results at varying moisture content levels. Notably, following the attainment of peak force, a distinct drop is observed, indicating a sudden crack jump at the specimen's interface. The occurrence of crack jump was also reported by Koloor et al. [50]. Such event could be attributed to two primary reasons. Firstly, stable crack propagation typically requires a 13 μm-thick Teflon film [51]. However, in the experiments conducted, a 15 μm-thick Teflon film was used. Secondly, for stable crack propagation, Carlsson et al. [52] recommended initial crack length to half span length ratio, a_o/L to be greater than 0.7. Nevertheless, in the experimental setup, the ratio was 0.42. The numerical simulations, employing

$\Gamma = 0.99$, demonstrate a close alignment with experimental data in terms of peak force, slope, and displacement at failure. The maximum difference, approximately 13%, is noted, with an exception for one specimen at $M = 3.8\%$. Given the singular occurrence of this deviation, it can reasonably be attributed to experimental scatter.

It is crucial to highlight that utilising BTSL ($\Gamma = 0$) would result in even larger discrepancies in the peak force and displacement at failure. Therefore, the adoption of the TTSL with a suitable choice of Γ proves essential in ensuring a satisfactory numerical simulation response across all moisture content levels in this study.

5.4. Cohesive zone length

The condition required to obtain accurate numerical results using CZM is the interface strength in the cohesive zone must be characterised properly by the finite element spatial discretisation where the number of elements of the cohesive zone is [53]:

$$N_e = \frac{L_{CZ}}{L_e} \tag{8}$$

In Equation (8), L_e represents the mesh size in the direction of crack propagation, while L_{CZ} denotes the length of the cohesive zone at the point of the first element failure, ensuring accurate capture of the cohesive stress distribution. Fig. 11 illustrates the assumed traction profile along the crack path for the initial five elements preceding the crack tip when the first element has undergone complete failure, resulting in a traction value of zero. The second element exhibits a traction lower than $t_{u,II}$ as it is in the softening region. The third and fourth elements share the same traction, corresponding to the plateau region. However, it is essential to note that the third element has experienced damage ($0 < D < 1$), while the damage initiation has just occurred for the fourth element ($D = 0$). As for the fifth element, it remains in the elastic region, where the element is still intact.

The cohesive zone length, L_{CZ} is determined by measuring the distance between the first element at the moment of complete failure ($D = 1$) and the element reaching the maximum traction, where damage initiation is observed ($D = 0$). For the TTSL depicted in Fig. 11, this refers to the distance between the first and fourth elements. It's important to emphasise that the variation of traction within elements 1–3 and 4–5 is an assumption made for illustrative purposes, necessitating further validation.

In Fig. 12(a)–(d), the distribution of mode II traction against the distance from the crack tip at the moment of complete failure of the first interface element, which represents the L_{CZ}, is illustrated. The final data in each plot represents the element that has just attained damage initiation ($D = 0$). Notably, in these plots, the mode II traction for the first three elements from the crack tip is consistently 0 MPa before sharply increasing to the respective shear interface strength. This observation suggests that, at the moment the first element experiences total failure, the crack extension is so abrupt that it directly propagates to the first three elements.

A minimum number of elements N_e within the cohesive zone is crucial for accurately representing the fracture energy, ensuring the model captures the continuum field of a cohesive crack [54]. Previous studies have generally indicated that this minimum N_e often ranges from 2 to 10 [54]. Further investigations that considered different modes of loading and adopted BTSL in numerical analysis suggested a minimum N_e of 3 for accurate analysis [55]. Recent findings aligned with this, emphasising that at least 3 cohesive elements within the cohesive zone are necessary to obtain an accurate cohesive zone length [14].

As indicated in Table 4, L_{CZ} ranges from 2.0 mm to 2.4 mm when employing TTSL across all moisture levels, with a given mesh size, L_e of 0.1 mm. Thus, based on Equation (8), the corresponding N_e falls within the range of 20–24, as detailed in Table 4. Notably, for TTSL, plasticity is induced when the shear interface strength is reached, signifying a plateau in the softening region. As a result, the expected N_e is higher compared to BTSL at the same mesh size, L_e and shear interface strength, $t_{u,II}$.

5.5. Crack growth profile

The crack growth profile is defined by key failure variables, specifically encompassing damage initiation ($0 < D < 1$) and complete damage ($D = 1$). Extracting data from force-displacement measurements in Fig. 10, the failure variables during the peak force timeframe imposed on ENF models under various moisture conditions are extracted. Considering symmetry, only half of the specimen's width in the delamination zone of interest is considered, as highlighted in yellow in Fig. 13. Analysis reveals that, at the peak force, the cohesive elements preceding the crack tip undergo complete damage, illustrated by the crack propagation length (depicted in black) in Fig. 14. The red region signifies the crack initiation length, while the blue region remains undamaged. At the point of peak force, the crack propagation length ranges from 0.5 mm to 0.6 mm, while the crack initiation length spans from 2.3 mm to 2.4 mm at the interface, irrespective of the moisture content in the ENF specimen.

The plastic zone's shape during interlaminar delamination of carbon/epoxy laminate is characterised by the extent of damage initiation. A comparative analysis of the interface damage initiation sizes reveals that, during this process, the size of damage initiation at the edge (under plane stress condition) is marginally larger than the size observed at mid-width (under plane strain condition). This discrepancy is attributed to plane strain condition restraining yielding, ultimately leading to a more confined or smaller plastic zone [56].

6. Conclusions

In this study, trapezoidal traction-separation law (TTSL) was implemented to simulate the mode II delamination behaviour in unidirectional carbon/epoxy composite laminates across moisture content levels of 0, 2.2, 3.8, and 5.3 %. Key findings and conclusions include:

i) TTSL with pseudo-plasticity $\Gamma = 0.99$ consistently outperformed BTSL ($\Gamma = 0$) in predicting force-displacement responses across all moisture conditions.
ii) The residual property model (RPM) demonstrated a strong fit for G_{IIC} as a function of moisture content. This modified RPM also exhibited an excellent fit for other cohesive parameters.
iii) Across all four moisture content levels, the cohesive zone length ranged from 2.0 to 2.4 mm.
iv) At the peak load, progressive damage of 2.3–2.4 mm and complete damage of 0.5–0.6 mm were observed for all moisture-conditioned cases.

Funding

The article processing charge for open-access publication is supported by Universität der Bundeswehr München.

Declaration of competing interest

The authors declare that they have no known competing financial interests or personal relationships that could have appeared to influence the work reported in this paper.

Acknowledgements

The authors highly acknowledge the financial support from the Ministry of Higher Education under Fundamental Research Grant Scheme, UTM, FRGS/1/2022/TK10/UTM/02/27 (R. J130000.7851.5F517) and Universiti Teknologi Malaysia under UTMFR

grant, Q.J130000.3851.21H92. Also, the authors appreciate the support of Chair of Composite Materials and Technical Mechanics, Faculty of Mechanical Engineering, Universität der Bundeswehr München through the project "Development of Concept and Materials for Space-adapted Hydrogen Tank and Efficient Integration into Aircraft", under the guidance of German Aerospace Center (DLR), which is financed by the "Bundesministeriums für Wirtschaft und Klimaschutz" - registration number 20E2204C. The financial support by Universität der Bundeswehr München for Open Access publication is acknowledged.

References

[1] Mlýnek J, et al. Fabrication of high-quality polymer composite frame by a new method of fiber winding process. Polymers 2020;12(5):1037.
[2] Deng J, et al. Review and assessment of fatigue delamination damage of laminated composite structures. Materials 2023;16(24):7677.
[3] Joshani M, Koloor S, Abdullah R. Damage mechanics model for fracture process of steel-concrete composite slabs. Appl Mech Mater 2012;165:339–45.
[4] Zhang J, et al. Effect of the cohesive law shape on the modelling of adhesive joints bonded with brittle and ductile adhesives. Int J Adhesion Adhes 2018;85:37–43.
[5] Xu Y, et al. A unified cohesive zone model for simulating adhesive failure of composite structures and its parameter identification. Compos Struct 2017;182:555–65.
[6] Chaves FJP, et al. Fracture mechanics tests in adhesively bonded joints: a literature review. J Adhes 2014;90(12):955–92.
[7] Low KO, et al. Mode I delamination behaviour of carbon/epoxy composite at different displacement rates. Compos B Eng 2019;176:107293.
[8] Low KO, et al. Displacement rate effects on the mode II shear delamination behavior of carbon fiber/epoxy composites. Polymers 2021;13(11).
[9] Low KO, et al. Displacement rate effects on mixed-mode I/II delamination of laminated carbon/epoxy composites. Polym Test 2022;108:107512.
[10] Wong KJ, et al. Moisture absorption effects on mode II delamination of carbon/epoxy composites. Polymers 2020;12(9).
[11] Johar M, et al. Numerical simulation methodology for mode II delamination of quasi-isotropic quasi-homogeneous composite laminates. J Compos Mater 2017;51(28):3955–68.
[12] Naghipour P, et al. Effect of fiber angle orientation and stacking sequence on mixed mode fracture toughness of carbon fiber reinforced plastics: numerical and experimental investigations. Mater Sci Eng, A 2010;527(3):509–17.
[13] Naghipour P, Bartsch M, Voggenreiter H. Simulation and experimental validation of mixed mode delamination in multidirectional CF/PEEK laminates under fatigue loading. Int J Solid Struct 2011;48(6):1070–81.
[14] Zhao L, et al. Simulation of delamination growth in multidirectional laminates under mode I and mixed mode I/II loadings using cohesive elements. Compos Struct 2014;116:509–22.
[15] Machado JJM, et al. Mode I fracture toughness of CFRP as a function of temperature and strain rate. J Compos Mater 2016;51(23):3315–26.
[16] Machado JJM, et al. Mode II fracture toughness of CFRP as a function of temperature and strain rate. Compos B Eng 2017;114:311–8.
[17] Sarrado C, et al. Assessment of energy dissipation during mixed-mode delamination growth using cohesive zone models. Compos Appl Sci Manuf 2012;43(11):2128–36.
[18] Harper PW, Sun L, Hallett SR. A study on the influence of cohesive zone interface element strength parameters on mixed mode behaviour. Compos Appl Sci Manuf 2012;43(4):722–34.
[19] Mollón V, et al. Finite element modelling of mode I delamination specimens by means of implicit and explicit solvers. Polym Test 2012;31(3):404–10.
[20] Chow ZP, et al. Thermal delamination modelling and evaluation of aluminium–glass fibre-reinforced polymer hybrid. Polymers 2021;13(4):492.
[21] Chandra N, et al. Some issues in the application of cohesive zone models for metal–ceramic interfaces. Int J Solid Struct 2002;39(10):2827–55.
[22] Al-Azzawi ASM, Kawashita LF, Featherston CA. Predicting interlaminar damage behaviour of fibre-metal laminates containing adhesive joints under bending loads. J Reinforc Plast Compos 2021;41(5–6):167–86.
[23] Al-Azzawi ASM, Kawashita LF, Featherston CA. A modified cohesive zone model for fatigue delamination in adhesive joints: numerical and experimental investigations. Compos Struct 2019;225:111114.
[24] Noruzi M, Khoramishad H. An equivalent cohesive zone model for a wide range of ductile and brittle adhesives. Fatig Fract Eng Mater Struct 2023;46(10):3939–52.
[25] de Moura MFSF, et al. Cohesive and continuum mixed-mode damage models applied to the simulation of the mechanical behaviour of bonded joints. Int J Adhesion Adhes 2008;28(8):419–26.
[26] Moreira RDF, et al. Mode II fracture characterisation of a honeycomb/carbon-epoxy sandwich panel using the asymmetric end-notched flexure test. J Sandw Struct Mater 2022;24(7):2030–46.
[27] de Moura MFSF, Campilho RDSG, Gonçalves JPM. Crack equivalent concept applied to the fracture characterization of bonded joints under pure mode I loading. Compos Sci Technol 2008;68(10–11):2224–30.
[28] de Moura MFSF, Campilho RDSG, Gonçalves JPM. Pure mode II fracture characterization of composite bonded joints. Int J Solid Struct 2009;46(6):1589–95.
[29] de Moura MFSF, et al. Mixed-mode I+II fracture characterization of a hybrid carbon-epoxy/cork laminate using the Single-Leg Bending test. Compos Sci Technol 2017;141:24–31.
[30] Gutkin R, et al. Modelling the R-curve effect and its specimen-dependence. Int J Solid Struct 2011;48(11–12):1767–77.
[31] de Morais AB. A new fibre bridging based analysis of the Double Cantilever Beam (DCB) test. Compos Appl Sci Manuf 2011;42(10):1361–8.
[32] Morais ABd. Beam analysis of the double cantilever beam specimen with fibre bridging. J Compos Mater 2014;49(14):1681–8.
[33] Heidari-Rarani M, Shokrieh MM, Camanho PP. Finite element modeling of mode I delamination growth in laminated DCB specimens with R-curve effects. Compos B Eng 2013;45(1):897–903.
[34] Wong KJ, Chong WWF, Goh K-L. Fiber bridging mechanism in moisture-induced mode I delamination in carbon/epoxy composites: finite element analysis and experimental investigation. Polym Compos 2023;44(2):1392–407.
[35] de Morais AB. Determination of the shear traction-separation law of adhesive layers using the end-notched flexure specimen. Eng Fract Mech 2020;235:107199.
[36] Chen J. Predicting progressive delamination of stiffened fibre-composite panel and repaired sandwich panel by decohesion models. J Thermoplast Compos Mater 2002;15(5):429–42.
[37] Allix O, Corigliano A. Modeling and simulation of crack propagation in mixed-modes interlaminar fracture specimens. Int J Fract 1996;77(2):111–40.
[38] Abdel-Monsef S, et al. Accurate simulation of delamination under mixed-mode loading using a multilinear cohesive law. Eng Fract Mech 2023;284:109233.
[39] May M, Voß H, Hiermaier S. Predictive modeling of damage and failure in adhesively bonded metallic joints using cohesive interface elements. Int J Adhesion Adhes 2014;49:7–17.
[40] Tauheed M, Datla NV. Characterization and prediction of hygrothermally aged CFRP adhesive joint subjected to mode II load. Composites Part C: Open Access 2023;11:100357.
[41] Anyfantis KN, Tsouvalis NG. Experimental and numerical investigation of Mode II fracture in fibrous reinforced composites. J Reinforc Plast Compos 2011;30(6):473–87.
[42] Ghabezi P, Farahani M. Trapezoidal traction–separation laws in mode II fracture in nano-composite and nano-adhesive joints. J Reinforc Plast Compos 2018;37(11):780–94.
[43] Khan MS, et al. Representative cell analysis for damage-based failure model of polymer hexagonal honeycomb structure under the out-of-plane loadings. Polymers 2020;13(1):52.
[44] Khan SA, et al. A fatigue model to predict interlaminar damage of FRP composite laminates subjected to mode I load. Polymers 2023;15(3):527.
[45] Watson B, et al. Mode I traction-separation measured using rigid double cantilever beam applied to structural adhesive. J Adhes 2020;96(8):717–37.
[46] Moslemi-Abyaneh B, Ghasemi AR. Thermal cycling effects on the mode-I delamination of multilayer laminated composites: an experimental-numerical approach. J Compos Mater 2023;57(24):3841–52.
[47] Johar M, et al. Effects of moisture absorption on the different modes of carbon/epoxy composites delamination. Polym Degrad Stabil 2019;165:117–25.
[48] Koloor S, Abdul-Latif A, Tamin MN. Mechanics of composite delamination under flexural loading. Key Eng Mater 2011;462:726–31.
[49] Mad Asasaari SF, et al. Moisture absorption effects on the mechanical properties of carbon/epoxy composites. International Journal of Structural Integrity 2020;11(4):605–14.
[50] Koloor SSR, Tamin MN. Mode-II interlaminar fracture and crack-jump phenomenon in CFRP composite laminate materials. Compos Struct 2018;204:594–606.
[51] ASTM D7905. Standard test method for determination of the mode II interlaminar fracture toughness of unidirectional fiber-reinforced polymer matrix composites. West Conshohocken, Pennsylvania, United States: ASTM International; 2014.
[52] Carlsson LA, Gillespie JW, Pipes RB. On the analysis and design of the end notched flexure (ENF) specimen for mode II testing. J Compos Mater 1986;20(6):594–604.
[53] Turon A, et al. Accurate simulation of delamination growth under mixed-mode loading using cohesive elements: definition of interlaminar strengths and elastic stiffness. Compos Struct 2010;92(8):1857–64.
[54] Turon A, et al. An engineering solution for solving mesh size effects in the simulation of delamination with cohesive zone models. Eng Fract Mech 2005;74(10):1665–82.
[55] Harper PW, Hallett SR. Cohesive zone length in numerical simulations of composite delamination. Eng Fract Mech 2008;75(16):4774–92.
[56] Anderson TL. Fracture mechanics: fundamentals and applications. CRC press; 2017.